Diffusive–Dispersive and Reactive Fronts in Porous Media

Iron(II) Oxidation at the Unsaturated–Saturated Interface

Haberer, Christina M. ; Muniruzzaman, Muhammad; Grathwohl, Peter ; Rolle, Massimo

Published in:
Vadose Zone Journal

Link to article, DOI:
10.2136/vzj2014.07.0091

Publication date:
2015

Document Version
Peer reviewed version

This is a Post Print of the article published on line 23rd February 2015 and printed July 2015 in Vadose Zone Journal, 14, No. 5. The publishers' version is available at the permanent link: doi: 10.2136/vzj2014.07.0091

Diffusive/Dispersive and Reactive Fronts in Porous Media: Fe(II)-Oxidation at the Unsaturated/Saturated Interface

Christina M. Haberer[1]*, Muhammad Muniruzzaman[1], Peter Grathwohl[1], Massimo Rolle[1,2,3]

[1]Center for Applied Geoscience, University of Tübingen, Hölderlinstrasse 12, D-72074 Tübingen, Germany
[2]Department of Civil and Environmental Engineering, Stanford University, 473 Via Ortega, 94305, Stanford, CA, USA
[3]Department of Environmental Engineering, Technical University of Denmark, Miljøvej Building 115, DK-2800 Lyngby, Denmark
*corresponding author: christina.haberer@uni-tuebingen.de

Impact Statement

Using a combined experimental and modeling approach we investigate the coupling between diffusive/dispersive processes and kinetic iron(II) oxidation in batch, 1-D column, and 2-D flow-through systems.

Abstract

Diffusive/dispersive mass transfer is important for many groundwater quality problems as it drives the interaction between different reactants, thus influencing a wide variety of biogeochemical processes. In this study we performed laboratory experiments to quantify oxygen transport in porous media, across the unsaturated/saturated interface, under both conservative and reactive transport conditions. As reactive system we considered the abiotic oxidation of ferrous iron in the presence of oxygen. We studied the reaction kinetics in batch experiments and its coupling with diffusive and dispersive transport processes by means of 1-D columns and 2-D flow-through experiments, respectively. A non-invasive optode technique was used to track oxygen transport into the initially anoxic porous media at highly resolved spatial and temporal scales. The results show significant differences in the propagation of the conservative and reactive oxygen fronts. Under reactive conditions oxygen, continuously provided from the atmosphere, was considerably retarded due to the interaction with dissolved iron(II), initially present in the anoxic groundwater. The reaction between dissolved oxygen and ferrous iron led to the formation of an iron(III) precipitation zone in the experiments. Reactive transport modeling based on a kinetic PHREEQC module tested in controlled batch experiments allowed a quantitative interpretation of the experimental results in both 1-D and 2-D setups.

Keywords: diffusion; transverse dispersion; unsaturated/saturated interface; iron(II) oxidation; porous media.

In natural systems, the geochemical and biological activity at the interface between different compartments, such as the unsaturated and the saturated zone in the subsurface, is determined by the fluxes and exchange rates across the interface. Interface regions are highly active in terms of physicochemical and microbiological processes (e.g., Sobolev and Roden, 2001; Bauer et al., 2009; Jost et al., 2014). A number of experimental and modeling studies have identified diffusive and dispersive processes as key mechanisms for mass transfer of volatile compounds to or from groundwater systems (e.g., Barber and Davis, 1987; Barber et al., 1990; McCarthy and Johnson, 1993; Klenk and Grathwohl, 2002; Werner and Höhener, 2002; Prommer et al., 2009; Haberer et al., 2011, 2012; Freitas et al., 2011).

Of particular importance is the mass transfer of oxygen to anoxic groundwater since dissolved oxygen plays a key role for many biogeochemical processes. The supply of oxygen influences the subsurface redox conditions and the rates of many biological and geochemical reactions (e.g., Stumm and Morgan, 1996; Chapelle, 2001; Mächler et al., 2013; Rezanezhad et al., 2014). The importance of oxygen transport across the capillary fringe has been shown in detailed experimental and modeling studies focusing on conservative transport (e.g., Williams and Oostrom, 2000; Haberer et al., 2011, 2014a, 2014b), microbially-mediated reactions (e.g., Sobolev and Roden, 2001; Maier et al., 2007; Dobson et al., 2007; Jost et al., 2014), and abiotic reactions (Farnsworth et al., 2012). The objective of this work is the simultaneous investigation of diffusive/dispersive oxygen transport under conservative and reactive conditions. As a reactive system we selected the abiotic oxidation of ferrous iron that is a process of great environmental relevance in shallow groundwater systems (e.g., Sung and Morgan, 1980; Appelo et al., 1999; Appelo and Postma, 2005; Martin, 2005; Vencelides et al., 2007). In fact, iron(II) oxidation affects the mobility and fate of many organic and inorganic contaminants. One notable example is the coupling of iron cycling with arsenic release and transport (e.g., Smedley and Kinniburgh, 2002; Stollenwerk, 2003; Wallis et al., 2011; Sharma et al., 2011; Voegelin et al., 2014). Dissolved ferrous iron is a common constituent of anoxic groundwater and, when it comes into contact with dissolved oxygen, it is oxidized to ferric iron. Once ferric iron is formed it readily undergoes hydrolysis and precipitates as solid ferric hydroxides ($Fe(OH)_3$). With time, ferric hydroxides are transformed into progressively more stable and crystalline minerals such as maghemite, lepidocrocite, hematite, and goethite (e.g., Sung and Morgan, 1980; Cornell and Schwertmann, 2003; Martin, 2005; Voegelin et al., 2010), which are the principal forms of mineralized ferric iron found in soils and aquifer sediments. Changes in redox and pH conditions influence iron speciation as well as the kinetics of iron(II) oxidation (Stumm and Morgan, 1996; Frini and Maaoui, 1997).

In this study, we experimentally investigate the coupling of abiotic iron(II) oxidation and transport processes in porous media. We focus on the interface between the unsaturated and the saturated zone and we perform (*i*) reactive batch experiments to characterize the kinetics of iron(II) oxidation under different

pH conditions and in the presence and absence of a catalyzer; (ii) 1-D conservative and reactive column experiments to investigate the propagation of oxygen fronts under diffusive conditions; and (iii) 2-D flow-through experiments to quantify oxygen transfer across the capillary fringe and the propagation of conservative and reactive fronts under advection-dominated flow-through conditions. Numerical transport simulations have been carried out to interpret the experimental results and to assess the implications of the experimental findings at larger temporal and spatial scales.

THEORETICAL BACKGROUND

Diffusive/Dispersive Transport in Porous Media

A correct description of diffusive/dispersive processes in porous media is of primary importance since these physical processes determine the transport and distribution of chemical species in the subsurface. Such processes are typically coupled and often limit the overall rate of biogeochemical reactions. In the absence of advective movement of groundwater, diffusion is the main process governing solute transport. In porous media, diffusion of a dissolved species is hindered by the reduced cross-sectional area available for the movement of solute molecules as well as by the size and the tortuous nature of the pores (e.g., Shackelford, 1991; Grathwohl, 1998; Appelo and Postma, 2005). In a 1-D porous medium diffusive transport of a conservative solute is described as:

$$\varepsilon \frac{\partial C(z,t)}{\partial t} = D_p \varepsilon \frac{\partial^2 C(z,t)}{\partial z^2} \qquad (1)$$

where C [M L^{-3}] is the concentration of the diffusing compound depending on distance, z [L], and time, t [T], ε [-] represents the porosity, and D_p [L T^{-2}] is the pore diffusion coefficient. The latter is related to the aqueous diffusivity of the dissolved species as well as to the properties of the porous medium by (e.g., Boudreau, 1996; Sabatini, 2000; Boving and Grathwohl, 2001; Delgado, 2006):

$$D_p = \frac{D_{aq}}{\tau} \approx D_{aq} \varepsilon^{m-1} \qquad (2)$$

where τ [-] is the tortuosity, a coefficient encompassing the effects of all geometrical and chemical interactions on the apparent diffusional constant in the porous medium (D_p) compared to that found in free aqueous solution, D_{aq} [L^2 T^{-1}] (Clennel, 1997). The right hand side of Eqn. 2 is a common empirical model relating the pore diffusion coefficient to the porosity of the packed bed (e.g., Epstein 1989; Boudreau, 1996; Grathwohl 1998; Boving and Grathwohl, 2001; Hu and Wang, 2003). m [-] is an empirical exponent for which different values have been reported in the literature. For instance, Peng et al. (2012) reported a value of 1.33 for soils, a range from 1.92-2.93 for limestone and sandstone, and a range from 2.5-5.4 for clays.

For the 1-D diffusion experiments at the unsaturated/saturated interface performed in this study, the following boundary conditions apply:

$$\begin{aligned} &C = C_{bg} \text{ at } t = 0 \text{ for } 0 < z \le \infty \\ &C = C_0 \text{ at } z = 0 \text{ for } t \ge 0 \\ &C = C_{bg} \text{ at } z \to \infty \text{ for } t \ge 0 \end{aligned} \tag{3}$$

Under these conditions, the analytical solution of the 1-D diffusion equation (Eqn. 1) is:

$$C_{norm} = \frac{C - C_{bg}}{C_0 - C_{bg}} = erfc\left(\frac{z}{2\sqrt{D_p t}}\right) \tag{4}$$

where the concentration of the diffusing compound is normalized by the background concentration prevailing in the porous medium, C_{bg} [M L^{-3}], and the concentration at the unsaturated/saturated interface, C_0 [M L^{-3}]. This analytical solution is used to analyze the results of the conservative transport experiments in the 1-D setup and to estimate the value of the pore diffusion coefficient.

Under flow-through conditions solute transport of a conservative species is determined by advective and dispersive processes. Considering a 2-D domain, the governing transport equation reads as:

$$\frac{\partial C}{\partial t} = D_L \frac{\partial^2 C}{\partial x^2} + D_T \frac{\partial^2 C}{\partial z^2} - v\frac{\partial C}{\partial x} \tag{5}$$

where v [L T^{-1}] is the seepage velocity, and D_L [L^2 T^{-1}] and D_T [L^2 T^{-1}] are the longitudinal and transverse components of the hydrodynamic dispersion tensor, respectively.

Mass transfer and mixing in the transverse direction are typically more important in subsurface transport problems (e.g., Kitanidis, 1994); particularly for a continuous release of dissolved species, as in the flow-through experiments performed in this study, for which the concentration gradients in the longitudinal direction become negligible compared to the ones in the transverse direction (e.g., Chiogna et al., 2011 and 2012). Thus, an accurate description of the transverse hydrodynamic dispersion coefficient is fundamental to properly describe dilution and reactive mixing processes. Recent pore-scale and laboratory studies have shown the important interplay between the fundamental physical processes of advection and diffusion not only at slow but also at high seepage velocities, resulting in compound-specific incomplete dilution in the pore channels (Rolle et al., 2012; Rolle and Kitanidis, 2014) and influencing the transport of uncharged polyatomic species as well as charged ions in porous media (Rolle et al., 2013a, Muniruzzaman et al., 2014). Such effects at the subcontinuum scale propagate and are relevant also at larger macroscopic scales (Rolle et al., 2013b). Hence, such effects need to be captured in dispersion parameterizations at the continuum scale. An example is the compound-specific model for transverse dispersion proposed by Chiogna et al. (2010). This parameterization of D_T, inspired by an earlier statistical model of Bear and Bachmat (1967), takes into account the influence of aqueous diffusion not only on the pore diffusion but also on the mechanical dispersion term:

$$D_T = D_p + D_{aq}\left(\frac{Pe^2}{Pe + 2 + 4\delta^2}\right)^{\beta} \quad (6)$$

where $Pe = vd/D_{aq}$ is the dimensionless grain Péclet number with d [L] representing the grain diameter, δ [-] is the ratio between the length of a pore channel and its hydraulic radius, and β [-] is an exponent accounting for incomplete dilution of the solute in the pore channels. Average values of $\delta = 6.2$ and $\beta = 0.5$ were determined experimentally considering a wide range of flow-through conditions in different porous media and were found in good agreement with the outcomes of pore-scale simulations (Rolle et al., 2012, Hochstetler et al., 2013).

In reactive systems coupled transport and biogeochemical transformation occurs. In the description of such systems, the reactive terms are included in the governing diffusion and advection-dispersion

equations (Eqs. 1 and 5). In this study we consider the abiotic oxidation of ferrous iron by dissolved oxygen, for which the reactive term is described in the following section.

Abiotic Iron(II) Oxidation

The abiotic oxidation of ferrous iron in the presence of oxygen is described by the following chemical reaction:

$$Fe^{2+} + 0.25O_2 + 2.5H_2O \rightarrow Fe(OH)_3(s) + 2H^+ \quad (7)$$

An intermediate step in this overall chemical reaction is the formation of ferric iron, which readily undergoes hydrolysis and precipitates as solid ferric hydroxide (Cornell and Schwertmann, 2003). Depending on the solution's pH and temperature, as well as on the ions participating in the reaction, the presence of organic constituents and oxidizing agents, various oxidation products are formed in different ratios (e.g., Stumm and Morgan, 1996; Voegelin et al., 2010). As an example, the slow oxidation of ferrous iron due to aeration can result in the formation of magnetite, lepidocrocite, hematite, and goethite (e.g., Frini and Maaoui, 1997). The oxidation of iron(II) (Eqn. 7) also results in the formation of H^+-ions and thus, depending on the buffering capability of the system, in a possible decrease of pH.

Due to the importance of iron(II) oxidation in many aquatic systems, the kinetics of this reactive process has been extensively studied. In aqueous solutions at pH $\geq$ 5 the oxygenation kinetics of ferrous iron follows the general rate law (e.g., Stumm and Lee, 1961; Sung and Morgan, 1980; Davison and Seed, 1983; Millero et al.1987; Stumm and Morgan, 1996):

$$-\frac{d[Fe^{2+}]}{dt} = k^*[Fe^{2+}][OH^-]^2 p_{O_2} \quad (8)$$

where k^* is the reaction rate constant for which Stumm and Morgan (1996) report a value of $8(\pm 2.5)\times 10^{13}$ mol^{-2} L^2 atm^{-1} min^{-1} at 20 °C. Expressing the dependence on oxygen as function of the dissolved aqueous concentration, the rate law reads as:

$$-\frac{d[Fe^{2+}]}{dt} = k[Fe^{2+}][OH^-]^2[O_2(aq)] \quad (9)$$

147 in which the reaction rate constant, *k*, now has units of $mol^{-3}\ L^{3}\ min^{-1}$.

148 According to Eqs. 8 and 9, the oxidation rate of ferrous iron is of first-order with respect to the
149 concentration of both ferrous iron and oxygen, whereas it is of second-order with respect to pH. Therefore,
150 the reaction rate is strongly pH-dependent, and below pH 6 the oxidation of ferrous iron is very slow (e.g.,
151 Martin, 2005; Morgan and Lahav, 2007). To increase the reaction rate catalysts, such as Cu^{2+} and Co^{2+},
152 may be added in trace quantities (Stumm and Lee, 1961; Stumm and Morgan, 1996).

153 Abiotic iron(II) oxidation may not only occur by direct oxidation of ferrous iron in the solution
154 (homogeneous reaction), but also by specific adsorption of ferrous iron to hydrous oxide surfaces (e.g.,
155 Stumm and Morgan, 1996; Park and Dempsey, 2005; Schmidt et al., 2009). Iron (hydr)oxides, formed as
156 reaction products in the homogeneous oxidation of iron(II), may further accelerate the reaction rate by
157 providing a surface for the autocatalytic oxidation. The autocatalytic oxidation process depends on the
158 amount of ferric iron (Wolthoorn et al., 2004) and is noticeable only for pH-values greater than about pH
159 7 (Sung and Morgan, 1980). At pH-values greater than 7 the oxidation of ferrous iron is a mixture of both
160 the homogeneous and the autocatalytic process with the former representing the dominating mechanism at
161 circumneutral pH (Wolthoorn et al., 2004). Hence, only the homogeneous reaction rate is considered in
162 this study to describe the abiotic oxidation of ferrous iron.

163

164 # MATERIAL AND METHODS

165 ## Experimental Setups

166 In the following, we present the different experimental setups used to investigate diffusive/dispersive and
167 reactive transport of oxygen at the interface between the unsaturated and the saturated zone. A schematic
168 overview is given in Fig. 1. We performed batch experiments, 1-D diffusion experiments, and 2-D flow-
169 through experiments in a thermostatic room at 22 °C.

170

171 < Figure 1 >

172

Batch experiments

Batch experiments were performed to characterize the abiotic iron(II)-oxidation reaction (Eqn. 7) and to determine the reaction rate constant needed for simulating reactive transport in the 1-D and 2-D experiments (*k* in Eqn. 9). In particular, we investigated the impact of pH and a catalyzer (Cu^{2+}) on the observed reaction rate. Table 1 summarizes the different conditions tested.

< Table 1 >

Before starting the experiments, four 250 mL-Schott bottles were equipped with an oxygen-sensitive sensor spot (SP-PSt3-NAU from PreSens GmbH, Regensburg, Germany). The sensor spot was attached to the inner wall of each Schott bottle to facilitate oxygen measurement during the experiment by applying a non-invasive optode technique (Fibox3 from PreSens GmbH, Regensburg, Germany; e.g., Haberer et al., 2011). Subsequently, the Schott bottles were filled with 250 mL air-equilibrated MilliQ water. To keep pH stable and to avoid mineral precipitation, an organic pH buffer (here: PIPES, CAS: 5625-37-6, with pK_a = 6.80 at 20 °C; Good et al., 1966) was added in experiments B, C, and D with a concentration of c(PIPES) = 1×10^{-3} mol L^{-1}. Complete dissolution of the pH buffer was achieved by heating up the solutions and allowing them to cool down to room temperature. To investigate the effect of a catalyzer we also added $CuSO_4$ to one of the Schott bottles (Batch D; $c(Cu^{2+}) = 3\times10^{-7}$ mol L^{-1} according to Stumm and Lee, 1961). If needed pH was adjusted to the desired initial pH-value with 1 mol L^{-1} NaOH. All Schott bottles were stirred continuously to achieve uniform distribution of the reactants and to enhance oxygen resupply from the atmosphere. After addition of Fe^{2+} as $FeCl_2{\cdot}4H_2O$ (CAS: 13478-10-9, final concentration: $c(Fe^{2+}) = 1.79\times10^{-4}$ mol L^{-1}), we followed $c(O_2)$, pH, $c(Fe^{2+})$, and $c(Fe_{tot})$ over time. During the experiment, the oxygen concentration was detected with an optical fiber from the outside, pH was measured with a pH-electrode (pH 540 GLP, WTW Wissenschaftlich-Technische Werkstätten GmbH, Weilheim, Germany), and water samples were taken to determine the concentrations of Fe^{2+} and Fe_{tot} by performing a ferrozine assay (Stookey, 1970; Viollier et al., 2000). To prevent oxidation of ferrous iron before the analysis, we

diluted the samples with 1 mol L^{-1} HCl in a 1:1 ratio. An additional dilution step, using multiwell plates, was necessary to measure c(Fe^{2+}) and c(Fe_{tot}). That is, 20 µL of the diluted sample were again mixed with either 80 µL HCl (c(HCl) = 1 mol L^{-1}) to measure ferrous iron, or 80 µL hydroxylamine hydrochloride solution (i.e., 10 % (m/v) hydroxylamine hydrochloride in 1 mol L^{-1} HCl) to measure total iron. 100 µL ferrozine solution (50 % (m/v) ammonium acetate with 0.1 % (m/v) ferrozine in MilliQ water) were added to each sample to measure the concentration of ferrous iron at a wavelength of 562 nm using a microplate reader (FLASHScan® 550 from Analytik Jena AG, Jena, Germany).

1-D diffusion experiments

Glass columns (length: 11.6 cm, inner diameter: 1.75 cm), filled with a fully water-saturated porous medium, were used to study diffusive conservative and reactive mass transfer of oxygen from the atmosphere to anoxic water (Fig. 1). In particular, we characterized pore diffusion in different porous media (i.e., in glass beads and in River Rhine sand with grain diameters of 0.4-0.6 mm) under conservative conditions and we investigated the impact of abiotic iron(II) oxidation on oxygen transport in 1-D reactive transport experiments, using the same conditions and reaction kinetics investigated in the batch systems (experiment B). In the conservative setup an initial solution identical to the one prepared for batch system B (Table 1), but without addition of ferrous iron, was used as pore water solution; in the reactive case we additionally added ferrous iron with a concentration of 1.79×10^{-4} mol L^{-1}. Such solutions were flushed with nitrogen and stored in Tedlar® gas sampling bags.

Before starting the experiment, we glued an oxygen-sensitive sensor strip (SP-PSt3-NAU from PreSens GmbH, Regensburg, Germany) with dimensions of 4.7 cm × 0.5 cm onto the inner wall of the glass column (Fig. 1) to obtain temporal and spatial profiles of oxygen concentration in one experimental run. The glass column was placed into a polystyrene box (Fig. 2) to minimize temperature effects and to keep humidity high, thus resulting in minimal evaporation rates and, hence, in the approximately constant location of the unsaturated/saturated interface. During the experiment temperature was recorded and used for temperature compensation of the measured oxygen concentrations. Moreover, the evaporation rate was

225 determined with a separate column (with same dimensions as the measurement column and filled with the
226 same fully water-saturated porous medium) based on weight measurements at the beginning and at the end
227 of the experiment.
228
229 < Figure 2 >
230
231 To prepare the setup the glass columns were closed on one end using screw caps with silicon/PTFE septa.
232 Before filling the measurement vial, we pierced hollow needles through the septum of the bottom screw
233 cap. The needles were connected to pump tubing, through which we injected the prepared anoxic solutions
234 into the column using a peristaltic pump (IPC 12, IDEX Health and Science GmbH, Wertheim, Germany).
235 Subsequently, the porous medium was filled into the column, always keeping the water table above the
236 upper limit of the porous medium packing. When the column was packed completely, a second cap was
237 screwed onto the measurement vial and a hollow needle was punched through the septum to facilitate
238 upward flow (Fig. 2). The anoxic solution was flushed through the system until a constant low background
239 concentration of oxygen was measured.
240 We started the experiment (time = 0) by switching off the inlet pump (no-flow condition), unscrewing the
241 upper cap, and removing the supernatant liquid in the measurement vial, such that the water meniscus,
242 representing the unsaturated/saturated interface, was at the upper limit of the porous medium packing.
243 Oxygen immediately started to diffuse into the anoxic porous medium (Fig. 2) and we measured the
244 breakthrough of oxygen concentrations at a specific point (13 mm) below the porous medium/atmosphere
245 interface as a function of time (10 s intervals). Additionally, every three to six hours the oxygen
246 distribution in the column was determined by measuring spatial profiles of oxygen concentration at high
247 resolution (2.5 mm) along the oxygen-sensitive sensor strip.
248
249

At the end of the experiment, we determined gravimetrically the porosity of the porous medium packing in the column:

$$\varepsilon = \frac{V_w}{V_{tot}} = \frac{\frac{m_w}{\rho_w}}{\frac{m_w}{\rho_w} + \frac{m_s}{\rho_s}} \quad (10)$$

where V_w [L^3] and V_{tot} [L^3] are the volumes of the water and the porous medium packing, m_w [M] and m_s [M] are the masses of the water and the solid phase, and ρ_w [M L^{-3}] and ρ_s [M L^{-3}] are the density of the water and the solid phase, respectively.

2-D flow-through experiments

Flow-through experiments were performed to investigate the propagation of dispersive oxygen fronts in a quasi 2-D setup. The flow-through chamber was constructed with two 5-mm thick glass panes, separated by a Viton® septum, and had inner dimensions of 16.2 cm (length, *L*) × 12.7 cm (height, *H*) × 0.5 cm (width, *W*). An oxygen-sensitive sensor strip was glued onto the inner wall of the chamber (at x = 13 cm from the inlet, see Fig. 1) to detect oxygen concentrations at high spatial resolution (2.5 mm spacing). We filled the flow-through chamber with glass beads with grain diameters of d = 0.4-0.6 mm. At the inlet and at the outlet of the chamber, hollow needles, connected to pump tubing (Fluran-HCA, ID 0.64 mm from IDEX Health & Science GmbH), were pierced through the Viton® septum separating the two glass panes. These needles were equally spaced by 0.75 cm, and served as inlet (12 ports) and outlet ports (13 ports) to induce a horizontal flow-field in the chamber during the experiment by means of two high-precision peristaltic pumps (IPC-N 24, IDEX Health & Science GmbH). An overview of the porous medium properties and of the flow and transport parameters in the 2-D setup is given in Table 2.

< Table 2 >

The conservative and reactive transport experiments were performed under the same conditions as the 1-D column systems, i.e., using anoxic buffered solutions without and with addition of ferrous iron, respectively (the latter solution corresponding to Batch B, Table 1). To minimize the contamination of the prepared anoxic solutions by atmospheric oxygen, after flushing the solutions with nitrogen, we added a small amount of ascorbic acid (CAS: 50-81-7) resulting in a concentration of 6.25×10^{-5} mol L^{-1}. Subsequently, the pH of the solutions was adjusted to the desired value of 7. Similarly, to minimize oxygen contamination on the long term of the flow-through experiments (days to weeks) we placed an AnaeroGen sachet (Fisher Scientific, Schwerte, Germany) in the gas phase of the glass bottles that were used to store the inlet solutions. The ascorbic acid in the sachet absorbed oxygen, which reduced the oxygen content in the gaseous phase to below 1 %. To extract water from the glass bottles and pump it in the flow-through setup, a thoroughly nitrogen-flushed Tedlar® gas sampling bag, serving as gas reservoir, was connected to the reservoir of the inlet anoxic solution (Fig. 1).

After flushing the system with at least two pore volumes, high-resolution vertical oxygen profiles were measured along the oxygen-sensitive sensor strip located close to the outlet of the flow-through chamber.

Modeling Approach

Numerical modeling was performed to quantitatively evaluate the experimental results in the batch, 1-D and 2-D systems. A reactive module for kinetic oxidation of ferrous iron was developed using the geochemical code PHREEQC-3 (Parkhurst and Appelo, 2013). The module was first developed for batch conditions and validated with the experimental dataset B (Table 1). The stoichiometry of ferrous iron oxidation was described as in the balanced redox reaction (Eqn. 7); the kinetics of iron(II) oxidation was implemented according to Eqn. 9. To simulate the reaction kinetics we decoupled the valence states of ferrous and ferric iron, following an approach similar to the one described in example 9 of Parkhurst and Appelo (2013), and we allowed the precipitation of ferrihydrite. Mimicking the experimental conditions, we used the same initial concentration of the major reactants (ferrous iron and dissolved oxygen) and a pH buffer with identical concentration and pKa of PIPES (Table 1). The only parameter that was adjusted was

299 the specific rate constant of iron(II) oxidation (k in Eqn. 9). To this end, we took advantage of the new
300 capabilities of the recently released IPHREEQC, and specifically of IPHREEQC-COM which allows
301 performing all geochemical PHREEQC calculations directly from MATLAB as well as from any other
302 software that can interface with a COM (component object model) server (Charlton and Parkhurst, 2011;
303 Wissmeier and Barry, 2011). Thus, an automatic fitting routine based on the trust-region-reflective
304 algorithm implemented in the MATLAB function lsqnonlin was used to determine the value of the
305 reaction rate constant through the minimization of the non-linear least squares problem between the
306 computed and measured concentrations.
307 The PHREEQC module for kinetic iron(II) oxidation was directly applied in the 1-D and 2-D systems.
308 The simulation of the diffusive/reactive transport in the 1-D column setup was performed in PHREEQC,
309 where the 10 cm saturated porous medium domain was discretized into 100 cells (Δz = 1 mm). The
310 simulations were performed for simulation times corresponding to the experimental duration and the
311 spatial and temporal profiles obtained from the model runs were compared to the experimental
312 measurements.
313 Flow and transport simulations were performed for the 2-D flow-through system. Since this and previous
314 experimental studies conducted using similar porous media (e.g., Haberer et al., 2011) have shown that a
315 sharp interface between the unsaturated and the underlying fully water-saturated zone can be identified,
316 and that steep oxygen gradients form only in the saturated zone, the system can be accurately described by
317 exclusively focusing on the fully water-saturated medium. Thus, we solved the flow problem using the
318 code MODFLOW (Harbaugh, 2005) and the transport problem with PHT3D (Prommer et al., 2003),
319 which couples the solute transport code MT3DMS (Zheng and Wang, 1999) with PHREEQC. The
320 geometry and the boundary conditions in the 2-D model closely represent the experimental setup and a
321 fine discretization (grid cells with Δx and Δz up to 0.5 and 0.25 mm, respectively) was used to allow
322 capturing the steep concentration gradients observed in the experimental setup.
323
324

RESULTS AND DISCUSSION

Batch Experiments

Batch experiments were performed to study the kinetics of iron(II) oxidation under different conditions. Figure 3 shows the time-dependent reduction in ferrous iron concentration for the batch experiments summarized in Table 1. In Batch A, no buffer was added to the solution and we measured a rapid decrease in pH from 7 to 5.5. This caused a significant decrease in the reaction rate, which strongly depends on pH (Eqs. 8 and 9), and thus only a slight decrease of the ferrous iron concentration was observed. In Batch B the pH was buffered and the results show a fast oxidation of iron(II) in the solution. Increasing the initial pH (Batch C) and adding $CuSO_4$ as catalyzer (Batch D) caused a further increase in the reaction rate and in the oxidation of dissolved ferrous iron.

< Figure 3 >

The conditions of Batch B were selected to investigate the impact of kinetic effects on reactive transport in the 1-D and 2-D experiments. Under these conditions, we measured the temporal evolution of dissolved ferrous iron concentration, oxygen, and pH over a time period of 80 min. The reactive PHREEQC module for kinetic iron(II) oxidation described above was used to simulate the experimental results and to directly obtain a best-fit value for the reaction rate constant (k). As shown in Fig. 4 a reasonably good agreement was found between the experimental data and the results of the simulations for the different parameters measured in the batch experiment. Furthermore, the automated fitting procedure implemented using the capability of IPHREEQC-COM yielded a value of the reaction rate constant of $k = 9.84(\pm 0.23)\times 10^{15}$ L^3 mol^{-3} s^{-1} (at 22 °C). This value is comparable with previously reported values of reaction rate constants for abiotic ferrous iron oxidation (e.g., Stumm and Lee, 1961; Davison and Seed, 1983; Stumm and Morgan, 1996).

< Figure 4 >

351 **1-D Oxygen Diffusive Fronts under Conservative and Reactive Conditions**

352 Oxygen diffusive fronts were tracked in the 1-D column setup, and conservative transport experiments
353 were performed in different porous media (i.e., in glass beads and River Rhine sand packings). Figure 5
354 shows the oxygen concentrations for a conservative diffusion experiment conducted in the 1-D column
355 setup using glass beads with grain diameters d = 0.4-0.6 mm as porous medium. The symbols represent
356 the measurements, whereas the continuous lines are the modeling results obtained by fitting the analytical
357 solution of the conservative 1-D transport problem (Eqn. 4) to the experimental data. The spatial profiles
358 measured at different time intervals along the oxygen-sensitive sensor strip show a progressive penetration
359 of the oxygen front into the anoxic porous medium (Fig. 5a). The breakthrough of oxygen at the
360 measurement location, 13 mm below the unsaturated/saturated interface, is shown in Fig. 5b.
361
362 < Figure 5 >
363
364 The simultaneous fitting of the analytical solution to the spatial and temporal profiles allowed us to
365 determine the value of the pore diffusion coefficient of oxygen in the packed column. We obtained a value
366 of $D_p = 1.18\times10^{-9}$ m^2 s^{-1}. Knowing the free aqueous diffusion coefficient for dissolved oxygen (Table 2)
367 the tortuosity of the porous medium can be estimated using Eqn. 2. We obtained a value of tortuosity of
368 1.67 for the column packed with glass beads and 1.73 for the one packed with river Rhine sand (Table 3).
369 These values compare well with previously reported results and also with estimates using an empirical
370 correlation with the packed bed porosity (Eqn. 2, right hand side), with an empirical exponent of m = 1.5
371 (e.g., Bruggeman 1935; Boudreau, 1996; Sabatini, 2000; Boving and Grathwohl, 2001; Delgado, 2006;
372 Coutelieris and Delgado, 2012).
373
374 < Table 3 >
375

We also performed a reactive experiment in the porous medium packed with glass beads with the aim of investigating the coupling of diffusive oxygen transport with the kinetic oxidation of ferrous iron. The oxygen concentration profiles measured along the oxygen-sensitive sensor strip at specific time intervals are presented in Fig. 6b. Reactive transport simulations were performed with a 1-D PHREEQC model including the pore diffusion coefficient determined in the conservative experiment (D_p = 1.18×10^{-9} m^2 s^{-1}) and the reaction rate constant obtained from the best fit analysis of the abiotic iron(II) oxidation in the batch system (k = 9.84×10^{15} mol^{-3} L^3 s^{-1}, Batch B). As can be observed in Fig. 6b, the pure forward modeling simulations of the reactive system using the experimentally determined transport and reaction parameters are in excellent agreement with the experimental data. In Fig. 6 we also included the spatial profiles of the conservative experiments in the same porous medium as well as the simulation outcomes of a hypothetical case of instantaneous reaction (Liu et al., 2010; Haberer et al., 2011), shown in Fig. 6a and Fig. 6c, respectively.

< Figure 6 >

The comparison between the spatial profiles for the three different cases presented in Fig. 6 is illustrative of the propagation of the oxygen fronts in the anoxic porous medium. The location of the oxygen fronts 18 hours after the start of the respective experiment is depicted for the three distinct cases. Due to the absence of a chemical reaction, the penetration depth of oxygen is largest for the conservative case and can be described by:

$$z_{cons} = 2erfc^{-1}(C_{norm})\sqrt{D_p t} \quad (11)$$

where erfc^{-1} is the inverse complementary error function. For C_{norm} = 0.05, D_p = 1.18×10^{-9} m^2 s^{-1}, and t = 18 h, the penetration depth was z_{cons} = 25 mm (Fig. 6a). Tracking the same normalized concentration, significantly smaller penetration depths were obtained in the reactive cases. The smallest penetration depth was found in the case of instantaneous reaction: $z_{reac,ins}$ = 17 mm. For the reactive transport

401 experiments with kinetic iron(II) oxidation, the oxygen profile reached a penetration depth of $z_{reac,kin}$ = 18
402 mm that is in-between the conservative and the instantaneous reaction cases, but closer to the latter.
403 The oxygen penetration depth at different times (also for C_{norm} = 0.05), corresponding to the measurement
404 of the spatial profiles in the conservative and reactive experiments, as well as the simulation results for the
405 three scenarios discussed above are reported in Fig. 7a. Considering the ratio of the penetration depth
406 increments over time we estimated the velocities of propagation of the oxygen fronts which appear to
407 follow a $1/\sqrt{t}$ -trend. The speed of propagation of the diffusive fronts is larger in the conservative case,
408 whereas for reactive transport the interaction with the dissolved ferrous iron results in the retardation of
409 the oxygen fronts.
410
411 < Figure 7 >
412
413 Figure 8 shows the temporal oxygen concentration profiles determined at 13 mm depth below the
414 unsaturated/saturated interface. The fastest propagation of the oxygen front in the conservative case is
415 reflected also by its earlier breakthrough compared to the observations in the reactive experiments. The
416 breakthrough curves in Fig. 8 also illustrate that the effect of the iron(II)-oxidation kinetics is significant at
417 early times when the experimental and simulated results are clearly distinct from the conservative and
418 instantaneous cases. However, as time progresses the oxygen breakthrough for the kinetic iron(II)
419 oxidation tends to approach the behavior of an instantaneous reaction.
420
421 < Figure 8 >
422
423 Numerical simulations were also performed to further investigate the propagation of conservative and
424 reactive oxygen fronts at spatial and temporal scales beyond the ones considered in the experiments. In
425 these scenarios, besides the three cases illustrated above, we also considered the kinetic oxidation of
426 ferrous iron in an unbuffered system (corresponding to Batch A in Table 1). The results are reported as

spatial profiles in Fig. 9. Over a time period of 0.5 days, comparable with the temporal scale of the 1-D diffusion experiments, the conservative, reactive instantaneous, and buffered reactive kinetic profiles are distinct, whereas the unbuffered reactive kinetic profile overlaps with the conservative case. As time increases (5, 50, and 500 days) the differences in the velocity of propagation of the oxygen fronts lead to increasingly different penetration depths. Moreover, the profiles for the buffered kinetic system tend to merge with the ones of the instantaneous reactive scenario since under these conditions the relatively fast reaction kinetics is limited by the diffusive transport. Conversely, kinetic effects start to be remarkable for the unbuffered kinetic reaction system at later time as shown by the spatial profiles in Fig. 9b (especially for t = 500 days). In fact, at later times the slow reaction kinetics, determined by the absence of pH buffering capacity, starts to have a noticeable effect and results in a slower propagation of the oxygen front compared to the conservative case.

< Figure 9 >

Oxygen Dispersive Fronts under Flow-Through Conditions

The impact of the kinetic iron(II)-oxidation reaction on oxygen transfer across the unsaturated/saturated interface was also investigated in a quasi 2-D flow-through system. In such setup we performed sequentially conservative and reactive experiments. First, the flow-through chamber, filled with glass beads with grain diameters in the range of d = 0.4-0.6 mm, was flushed with an anoxic solution, containing the pH-buffer but no ferrous iron, at an average flow velocity of 1.9 m d^{-1}. Due to the oxygen gradient between the atmosphere and the anoxic water phase, oxygen was transferred across the unsaturated/saturated interface into the anoxic water. After reaching steady state, we measured the vertical oxygen concentration profile for this conservative experiment at the oxygen-sensitive polymer strip located at x = 13 cm from the inlet. Successively, we performed the reactive experiment by injecting at the inlet an anoxic solution containing ferrous iron and the pH buffer. As can be observed in the photograph of Fig. 10a, the contact between dissolved oxygen and ferrous iron caused the precipitation of iron

hydroxides close to the unsaturated/saturated interface. The shape of the iron precipitation zone is also significantly influenced by the flow field in the flow-through system, as substantiated by the flow model and by the computed flow lines (Fig. 10b). Reactive transport was simulated by incorporating the kinetic geochemical PHREEQC module, previously applied in the batch and 1-D system, into the multidimensional transport simulator PHT3D (Prommer et al., 2003). The comparison of the experimental data and the outcome of forward simulations with the same reaction kinetics described above and with the key transport parameter, the local transverse hydrodynamic dispersion coefficient calculated according to Eqn. 6, is shown in Fig. 10c. Despite the limited spatial scale of the setup, a significant difference can already be appreciated between the spatial oxygen profiles in the conservative and reactive experiments. Similarly to the observations in the 1-D diffusion system, also in the flow-through setup the dispersive oxygen front penetrates further in the anoxic porous medium in the case of conservative transport.

< Figure 10 >

Figure 11 shows the penetration depth and the velocity of propagation of the dispersive oxygen fronts for two distinct seepage velocities: v = 1.9 m d^{-1} (as in the flow-through experiments) and for a scenario at lower flow velocity, v = 0.19 m d^{-1}. The symbols refer to the conservative and kinetic reactive cases and are plotted in the region of the flow-through domain where the flow is approximately horizontal. The penetration depths are larger and more distinct between the conservative and reactive cases for the low flow velocity scenario, due to the tenfold higher residence time of oxygen in the flow-through system. However, as can be observed in Fig. 11b, the velocity of propagation of the dispersive oxygen fronts is considerably larger for the case with higher seepage velocity.

< Figure 11 >

CONCLUSIONS

The quantitative understanding of mixing processes in porous media is of critical importance for many environmental applications. A challenging task is to address the coupling between transport and biogeochemical reactions in subsurface environments. This is particularly true for mixing-induced mineral precipitation, which typically occurs along multi-component chemical gradients in narrow mixing zones and at the interface between different compartments. An increasing number of recent studies have addressed the complexity of these reactive systems in porous media (e.g., Tartakovsky et al., 2008; Zhang et al., 2010; Yoon et al. 2012; Molins et al., 2012; Gebrehiwet et al., 2014; Redden et al., 2014). In this work we investigated the abiotic oxidation of ferrous iron resulting in the precipitation of ferric hydroxides at the interface between the unsaturated and the saturated zones. In particular, we focused on the effects of abiotic iron(II) oxidation on the propagation of oxygen fronts in diffusive transport regimes as well as under flow-through conditions. Through the direct comparison of conservative and reactive transport in the same setups, our experiments allow quantifying the significant influence of ferrous iron oxidation on the penetration depth and on the speed of propagation of oxygen fronts in anoxic, water-saturated porous media. We also show that the chemistry of the anoxic solution, and in particular its pH buffering capability, plays a significant role in the propagation of oxygen fronts and on the importance of the kinetics of abiotic iron(II) oxidation for reactive transport. In pH-buffered systems we found that the kinetics of iron(II) oxidation becomes less important with increasing time and that at larger time scales the reaction can be described as an instantaneous process. Conversely, the iron(II)-oxidation kinetics can be important also at large time scales in unbuffered systems, where the decrease in pH strongly affects the reaction rates. Thus, under these conditions the slow reaction rate may become the controlling factor in the coupling with typically slow, and thus rate-limiting, diffusive and dispersive processes. Although our study was performed under simplifying conditions compared to physical and chemical heterogeneous groundwater systems, the results on the coupling between transport processes and abiotic ferrous iron oxidation have important implications for relevant subsurface environmental processes such as transport of inorganic contaminants and their interaction with iron minerals (e.g., Smedley and Kinniburgh, 2002),

505 acidification of groundwater (e.g., Kjøller et al., 2004; Franken et al., 2009), pyrite oxidation (e.g.,
506 Prommer and Stuyfzand, 2005), formation of gley soils and oxidized iron mineral inclusions in open
507 framework gravel lenses in braided river sediments (e.g., Cornell and Schwertmann, 2003).
508 Finally, our experiments and their model-based interpretation also show that the accurate and independent
509 determination of key transport parameters (i.e., pore diffusion coefficient in the 1-D setups and the
510 transverse dispersion coefficient in the 2-D flow-through system) as well as the detailed study and
511 description of reaction kinetics allows the predictive use of numerical simulations for reactive systems
512 where transport and reactive processes are coupled.
513

514 **Acknowledgments**

515 This study was funded by the DFG (German Research Foundation) through the Research Group FOR 831
516 'Dynamic Capillary Fringes – A Multidisciplinary Approach' (grant GR971/22-1) and by the Baden-
517 Württemberg Stiftung through the Elite Program for Postdocs. M.R. acknowledges the support of the
518 Marie Curie International Outgoing Fellowship (DILREACT project) within the 7th European Community
519 Framework Program. The authors thank Wolfgang Kürner, Bernice Nisch, Ye Yu, and the
520 Geomicrobiology Group at the University of Tübingen (Department of Geosciences) for technical support
521 and Prof. S.B. Haderlein for helpful discussions.
522

523 **REFERENCES**

524 Appelo, C.A.J., B. Drijver, R. Hekkenberg, and M. de Jonge. 1999. Modeling in situ iron removal from ground
525 water. Ground Water 37(6):811-817.
526 Appelo, C.A.J., and D. Postma. 2005. Geochemistry, groundwater and pollution. 2nd ed. CRC Press.
527 Barber, C., and G.B. Davis. 1987. Volatilization of methane from groundwater: Laboratory simulation and field
528 investigations in a sand aquifer. In: Proceedings AWRC Conference "Groundwater Systems under Stress",
529 Brisbane, Australia. AWRC Conference Series 13:157-164.
530 Barber, C., G.B. Davis, D. Briegel, and J.K. Ward. 1990. Factors controlling the concentration of methane and other
531 volatiles in groundwater and soil-gas around a waste site. J. Contam. Hydrol. 5(2):155-169.

532 Bauer, R.D., M. Rolle, P. Kürzinger, P. Grathwohl, R.U. Meckenstock, and C. Griebler. 2009. Two-dimensional
533 flow-through microcosms - versatile test systems to study biodegradation processes in porous aquifers. J.
534 Hydrol. 369:284-295. doi:10.1016/j.jhydrol.2009.02.037.
535 Bear, J., and Y. Bachmat. 1967. A generalized theory on hydrodynamic dispersion in porous media. In: IASH
536 symposium on artificial recharge and management of aquifers, Haifa, Israel 72:7-16.
537 Boudreau, B.P. 1996. The diffusive tortuosity of fine-grained unlithified sediments. Geochim. Cosmochim. Ac.
538 60(16):3139-3142.
539 Boving, T., and P. Grathwohl. 2001. Tracer diffusion coefficients in sedimentary rocks: Correlation to porosity and
540 hydraulic conductivity. J. Contam. Hydrol. 53(1-2):85-100.
541 Bruggeman, D.A.G. 1935. Berechnung verschiedener physikalischer Konstanten von heterogenen Substanzen. I.
542 Dielektrizitätskonstanten und Leitfähigkeiten der Mischkörper aus isotropen Substanzen. Ann. Ph. Leipzig.
543 416(7):636-664.
544 Chapelle, F.H. 2001. Ground-water microbiology and geochemistry. 2nd ed. John Wiley & Sons, New York.
545 Charlton, S. R., and D.L. Parkhurst. 2011. Modules based on the geochemical model PHREEQC for use in scripting
546 and programming languages. Comput. Geosci. 37(10):1653-1663. doi:10.1016/j.cageo.2011.02.005.
547 Chiogna, G., C. Eberhardt, P. Grathwohl, O.A. Cirpka, and M. Rolle. 2010. Evidence of compound-dependent
548 hydrodynamic and mechanical transverse dispersion by multitracer laboratory experiments. Env. Sci. Technol.
549 44(2):688-693. doi:10:1021/es9023964.
550 Chiogna, G., O.A. Cirpka, P. Grathwohl, and M. Rolle. 2011. Relevance of local compound-specific transverse
551 dispersion for conservative and reactive mixing in heterogeneous porous media. Water Resour. Res.
552 47:W07540. doi:10.1029/2010WR010270.
553 Chiogna, G., D.L. Hochstetler, A. Bellin, P.K. Kitanidis, and M. Rolle. 2012. Mixing, entropy and reactive solute
554 transport. Geophys. Res. Lett. 39:L20405. doi:10.1029/2012GL053295.
555 Clennel, M.B. 1997. Tortuosity: A guide through the maze. In: Developments in Petrophysics. Ed. Lovell, M.A., and
556 P.K. Harvey. Geol. Soc. Special Publication 122:299-344.
557 Cornell, R.M., and U. Schwertmann. 2003. The iron oxides: Structure, properties, reactions, occurences and uses. 2nd
558 Ed. Wiley-VCH, ISBN 3-527-30274-3.
559 Coutelieris, F.A., and J.M.P.Q. Delgado. 2012. Transport processes in porous media. Springer, ISBN 978-3-642-
560 27909-6.

561 Davison, W., and G. Seed. 1983. The kinetics of the oxidation of ferrous iron in synthetic and natural waters.
562 Geochim. Cosmochim. Ac. 47:67-79.
563 Delgado, J.M.P.Q. 2006. A simple experimental technique to measure tortuosity in packed beds. Can. J. Chem. Eng.
564 84:651-655.
565 Dobson, R., M.H. Schroth, J. Zeyer. 2007. Effect of water-table fluctuations on dissolution and biodegradation of a
566 multi-component, light nonaqueous-phase liquid. J. Contam. Hydrol. 94:235-248.
567 Epstein, N. 1989. On the tortuosity and the tortuosity factor in flow and diffusion through porous media. Chem. Eng.
568 Sci. 44(3):777-779.
569 Farnsworth, C.E., A. Voegelin, and J.G. Hering. 2012. Manganese oxidation induced by water table fluctuations in a
570 sand column. Env. Sci. Technol. 46:277-284.
571 Franken, G., D. Postma, W.H.M. Duijisveld, J. Böttcher, and J. Molson. 2009. Acid groundwater in an anoxic
572 aquifer: Reactive transport modelling of buffering processes. Appl. Geochem. 24:890-899.
573 Freitas, J.G., B. Doulatyari, J.W. Molson, J.F. Barker. 2011. Oxygenated gasoline release in the unsaturated zone,
574 Part 2: Downgradient transport of ethanol and hydrocarbons. J. Contam. Hydrol. 125:70-85.
575 doi:10.1016/j.jconhyd.2011.05.002.
576 Frini, A., and E. Maaoui. 1997. Kinetics of the formation of goethite in the presence of sulfates and chlorides of
577 monovalent cations. J. Colloid Interface Sci. 190:269-277.
578 Gebrehiwet, T., L. Guo, D. Fox, Y. Fujita, R. Smith, J. Henriksen, and G. Redden. 2014. Precipitation of calcium
579 carbonate and calcium phosphate under diffusion controlled mixing. Appl. Geochem. 46:43-56.
580 Good, N.E., G.D. Winget, W. Winter, T.N. Connolly, S. Izawa, and R.M.M. Singh. 1966. Hydrogen ion buffers for
581 biological research. Biochemistry 5(2):467-477.
582 Grathwohl, P. 1998. Diffusion in natural porous media: Contaminant transport, sorption/desorption and dissolution
583 kinetics. Springer, ISBN 0-792-38102-5.
584 Haberer, C.M., M. Rolle, S. Liu, O.A. Cirpka, and P. Grathwohl. 2011. A high-resolution non-invasive approach to
585 quantify oxygen transport across the capillary fringe and within the underlying groundwater. J. Contam.
586 Hydrol. 122:26-39.
587 Haberer, C.M., M. Rolle, O.A. Cirpka, and P. Grathwohl. 2012. Oxygen transfer in a fluctuating capillary fringe.
588 Vadose Zone J. doi.10.2136/vzj2011.0056.

589 Haberer, C.M., O.A. Cirpka, M. Rolle, and P. Grathwohl. 2014a. Experimental sensitivity analysis of oxygen transfer
590 in the capillary fringe. Ground Water 52(1):37-49. doi:10.1111/gwat.12028.
591 Haberer, C.M., M. Rolle, O.A. Cirpka, and P. Grathwohl. 2014b. Impact of heterogeneity on oxygen transfer in a
592 fluctuating capillary fringe. Ground Water – *in press*. doi:10.1111/gwat.12149.
593 Harbaugh, A.W. 2005. MODFLOW-2005, the U.S. Geological Survey modular ground-water model – The Ground-
594 Water Flow Process. U.S. Geological Survey Techniques and Methods 6-A16. Reston, Virginia: USGS.
595 Hochstetler, D.L., M. Rolle, G. Chiogna, C.M. Haberer, P. Grathwohl, and P. Kitanidis. 2013. Effects of compound-
596 specific transverse mixing on steady-state reactive plumes: Insights from pore-scale simulations and Darcy-
597 scaly experiments. Adv. Wat. Resour. 54:1-10.
598 Hu, Q., and J.S.Y. Wang. 2003. Aqueous-phase diffusion in unsaturated geologic media: A review. Critical Reviews
599 in Env. Sci. Technol. 33(3):275-297.
600 Jost, D., C.M. Haberer, P. Grathwohl, J. Winter, and C. Gallert. 2014. Oxygen transfer in a fluctuating capillary
601 fringe: Impact of microbial respiratory activity. Vadose Zone J. – *submitted*.
602 Kitanidis, P. 1994. The concept of the dilution index. Water Resour. Res. 30(7):2011-2026.
603 doi:10.1029/94WR00762.
604 Kjøller, C., D. Postma, and F. Larsen. 2004. Groundwater acidification and the mobilization of trace metals in a
605 sandy aquifer. Env. Sci. Technol., 38(10):2829-2835.
606 Klenk, I.D., and P. Grathwohl. 2002. Transverse vertical dispersion in groundwater and the capillary fringe. J.
607 Contam. Hydrol. 58:111-128.
608 Liu, S., R. Liedl, and P. Grathwohl. 2010. Simple analytical solutions for oxygen transfer into anaerobic
609 groundwater. Water Resour. Res. 46:W10542. doi:10.1029/2009WR008434.
610 Mächler, L., S. Peter, M.S. Brennwald, and R. Kipfer. 2013. Excess air formation as a mechanism for delivering
611 oxygen to groundwater. Water Resour. Res. 49:6847-6856. doi:10.1002/wrcr.20547.
612 Maier, U., H. Rügner, and P. Grathwohl. 2007. Gradients controlling natural attenuation of ammonium. Appl.
613 Geochem. 22:2606-2617. doi:10.1016/j.apgeochem.2007.06.009.
614 Martin, S.T. 2005. Precipitation and dissolution of iron and manganese oxides. In: Environmental catalysis. Ed.
615 Grassian, V.H. CRC Press Boca Raton, 61-81.
616 McCarthy, K.A., and R.L. Johnson. 1993. Transport of volatile organic compounds across the capillary fringe. Water
617 Resour. Res. 29(6):1675-1683.

618 Millero, F.J., S. Sotolongo, and M. Izaguirre. 1987. The oxidation kinetics of Fe(II) in seawater. Geochim.
619 Cosmochim. Ac. 51:793-801.
620 Molins, S., D. Trebotich, C. Steefel, and C. Shen. 2012. An investigation of the effect of pore scale flow on average
621 geochemical reaction rates using direct numerical simulation. Water Resour. Res. 48:W03527.
622 doi:10.1029/2011WR011404.
623 Morgan, B., and O. Lahav. 2007. The effect of pH on the kinetics of spontaneous Fe(II) oxidation by O_2 in aqueous
624 solution: Basic principles and a simple heuristic description. Chemosphere 68:2080-2084.
625 Muniruzzaman, M., C.M. Haberer, P. Grathwohl, and M. Rolle. 2014. Multicomponent ionic dispersion during
626 transport of electrolytes in heterogeneous porous media: Experiments and model-based interpretation.
627 Geochim. Cosmochim. Ac. doi:10.1016/j.gca.2014.06.020.
628 Park, B., and B.A. Dempsey. 2005. Heterogeneous oxidation of Fe(II) on ferric oxide at neutral pH and a low partial
629 pressure of O_2. Env. Sci. Technol. 39(17):6494-6500.
630 Parkhurst, D.L., and C.A.J. Appelo. 2013. Description of input and examples for PHREEQC version 3 – A computer
631 program for speciation, batch-reaction, one-dimensional transport, and inverse geochemical calculations. U.S.
632 Geological Survey Techniques and Methods, book 6, chap. A43, 497 p., available only at
633 http://pubs.usgs.gov/tm/06/a43.
634 Peng, S., Q. Hu, and S. Hamamoto. 2012. Diffusivity of rocks: Gas diffusion measurements and correlation to
635 porosity and pore size distribution. Water Resour. Res. 48:W02507. doi:10.1029/2011WR011098.
636 Pollock, D.W. 1994. A particle tracking post-processing package for MODFLOW: The U.S. Geological Survey
637 finite-difference ground-water flow model. User's guide for modpath/modpath-plot, version 3. of 94-464, U.S.
638 Geol. Survey, Reston, VA.
639 Prommer, H., D.A. Barry, and C. Zheng. 2003. MODFLOW/MT3DMS-based reactive multicomponent transport
640 modeling. Ground Water 41(2):247-257.
641 Prommer, H., and P.J. Stuyfzand. 2005. Identification of temperature-dependent water quality changes during a deep
642 well injection experiment in a pyritic aquifer. Environ. Sci. Technol. 39(7):2200-2209.
643 Prommer, H., B. Anneser, M. Rolle, F. Einsiedl, and C. Griebler. 2009. Biogeochemical and isotopic gradients in a
644 BTEX/PAH contaminant plume: model-based interpretation of a high-resolution field data set. Environ. Sci.
645 Technol. 43:8206-8212. doi:10.1021/es901142a.

Redden, G., D. Fox, C. Zhang, Y. Fujita, L.J. Guo, and H. Huang. 2014. $CaCO_3$ Precipitation, transport and sensing in porous media with in situ generation of reactants. Environ. Sci. Technol. 48(1):542-549.

Rezanezhad, F., R.-M. Couture, R. Kovac, D. O'Connell, and P. Van Capellen. 2014. Water table fluctuations and soil biogeochemistry: An experimental approach using an automated soil column system. J. Hydrol. 509:245-256.

Rolle, M., D. Hochstetler, G. Chiogna, P.K. Kitanidis, and P. Grathwohl. 2012. Experimental investigation and pore-scale modeling interpretation of compound-specific transverse dispersion in porous media. Transp. Porous Med. 93:347-362. doi:10.1007/s11242-012-9953-8.

Rolle, M., Md. Muniruzzaman, C.M. Haberer, and P. Grathwohl. 2013a. Coulombic effects in advection-dominated transport of electrolytes in porous media: Multicomponent ionic dispersion. Geochim. Cosmochim. Ac. 120:195-205.

Rolle, M., G. Chiogna, D.L. Hochstetler, and P.K. Kitanidis. 2013b. On the importance of diffusion and compound-specific mixing for groundwater transport: An investigation from pore to field scale. J. Contam. Hydrol. 153:51-68. doi:10.1016/j.jconhyd.2013.07.006.

Rolle, M., and P.K. Kitanidis, 2014. Effects of compound-specific dilution on transient transport and solute breakthrough: A pore-scale analysis. Adv. Water Resour. doi:10.1016/j.advwatres.2014.06.012.

Sabatini, D.A. 2000. Sorption and intraparticle diffusion of fluorescent dyes with consolidated aquifer media. Ground Water 38(5):651-656.

Schmidt, C., L. Corbari, F. Gaill, and N. Le Bris. 2009. Biotic and abiotic controls on iron oxyhydroxide formation in the gill chamber of the hydrothermal vent shrimp *Rimicaris exoculata*. Geobiology 7:454-464.

Shackelford, C.D. 1991. Laboratory diffusion testing for waste disposal – A review. J. Contam. Hydrol. 7:177-217.

Sharma, P., M. Rolle, B. Kocar, S. Fendorf, and A. Kappler. 2011. Influence of natural organic matter on arsenic transport and retention. Env. Sci. Technol. 45:546-553.

Smedley, P.L., and D.G. Kinniburgh. 2002. A review of the source, behavior and distribution of arsenic in natural waters. Appl. Geochem. 17:517-568.

Sobolev, D., and E.E. Roden. 2001. Suboxic deposition of ferric iron by bacteria in opposing gradients of Fe(II) and oxygen at circumneutral pH. Appl. Environ. Microb. 67(3):1328-1334. doi:10.1128/AEM.67.3.1328-1334.2001.

674 Stollenwerk, K.G. 2003. Geochemical processes controlling transport of arsenic in groundwater: A review of
675 adsorption. In: Arsenic in Groundwater. Ed. Welch, A.H., and K.G. Stollenwerk. Kluwer Academic
676 Publishers Boston, 67-100.
677 Stookey, L.L. 1970. Ferrozine – A new spectrometric reagent for iron. Anal. Chem. 42(7):779-781.
678 Stumm, W., and G.F. Lee. 1961. Oxygenation of ferrous iron. Ind. Eng. Chem. 53:143-146.
679 Stumm, W., and J.J. Morgan. 1996. Aquatic chemistry: chemical equilibria and rates in natural waters. Jon Wiley
680 and Sons, New York.
681 Sung, W., and J.J. Morgan. 1980. Kinetics and product of ferrous iron oxygenation in aqueous systems. Env. Sci.
682 Technol. 14(5):561-568.
683 Tartakovsky, A.M., G.D. Redden, P.C. Lichtner, T.C. Scheibe, and P. Meakin. 2008. Mixing-induced precipitation:
684 Experimental study and multi-scale numerical analysis. Water Resour. Res.
685 44:W06S04. doi:10.1029/2006WR005725.
686 Vencelides, Z., O. Sracek, and H. Prommer. 2007. Iron cycling and its impact on the electron balance at a petroleum
687 hydrocarbon contaminated site in Hnevice, Czech Republic. J. Contam. Hydrol. 89:270-294.
688 Viollier, E., P.W. Inglett, K. Hunter, A.N. Roychoudhury, and P. Van Cappellen. 2000. The ferrozine method
689 revisited: Fe(II)/Fe(III) determination in natural waters. Appl. Geochem. 15:785-790.
690 Voegelin, A., R. Kaegi, J. Frommer, D. Vantelon, and S.J. Hug. 2010. Effect of phosphate, silicate, and Ca on
691 Fe(III)-precipitates formed in aerated Fe(II)- and As(III)-containing water studied by X-ray absorption
692 spectroscopy. Geochim. Cosmochim. Ac. 74(1):164-186. doi:10.1016/j.gca.2009.09.020.
693 Voegelin, A., R. Kaegi, M. Berg, K. Nitzsche, A. Kappler, V. Lan, P. Trang, J. Goettlicher, and R. Steininger. 2014.
694 Solid-phase characterization of an effective household sand filter for As, Fe, and Mn removal from
695 groundwater in Vietnam. Environ. Chem. – *in press*.
696 Wallis, I., H. Prommer, T. Pichler, V.E.A. Post, S. Norton, M. Annable, and C.T. Simmons. 2011. A process-based
697 reactive transport model to quantify arsenic mobility during aquifer storage and recovery of potable water.
698 Environ. Sci. Technol. 45(16):6924-6931.
699 Werner, D., and P. Höhener. 2002. The influence of water table fluctuations on the volatilization of contaminants
700 from groundwater. In: Groundwater quality: Natural and enhanced restoration of groundwater pollution:
701 Proceedings of GQ 2001, Sheffield, UK. June 2001. Ed. Thornton, S.F., and S.E. Oswald. IAHS Publ. 275.
702 Int. Assoc. Hydrol Sci., Wallingford, UK. p. 213-218.

703 Williams, M.D., and M. Oostrom, 2000. Oxygenation of anoxic water in a fluctuating water table system: An
704 experiment and numerical study. J. Hydrol. 230:70-85.
705 Wissmeier, L., and D.A. Barry. 2011. Simulation tool for variably saturated flow with comprehensive geochemical
706 reactions in two- and three-dimensional domains. Environ. Modell. Softw. 26(2):210-218.
707 doi:10.1016/j.envsoft.2010.07.005.
708 Wolthoorn, A., E.J.M. Temminghoff, L. Weng, and W.H. van Riemsdijk. 2004. Colloid formation in groundwater:
709 Effect of phosphate, manganese, silicate and dissolved organic matter on the dynamic heterogeneous
710 oxidation of ferrous iron. Appl. Geochem. 19:611-622.
711 Yoon H., A.J. Valocchi, C.J. Werth, and T. Dewers. 2012. Pore-scale simulation of mixing-induced calcium
712 carbonate precipitation and dissolution in a microfluidic pore network. Water Resour. Res. 48(2):W02524.
713 doi:10.1029/2011WR011192.
714 Zhang C., K. Dehoff, N. Hess, M. Oostrom, T.W. Wietsma, A.J. Valocchi, B.W. Fouke, and C.J. Werth. 2010. Pore-
715 scale study of transverse mixing induced $CaCO_3$ precipitation and permeability reduction in a model
716 subsurface sedimentary system. Environ. Sci. Technol. 44:7833-7838. doi:10.1021/es1019788.
717 Zheng, C., and P.P. Wang. 1999. MT3DMS: A modular three-dimensional multispecies model for simulation of
718 advection, dispersion, and chemical reactions of contaminants in groundwater systems. Documentation and
719 user's guide. Contract report SERDP-99-1. U.S. Army Engineer Research and Development Center,
720 Vicksburg, MS.

FIGURE CAPTIONS, TABLES, AND FIGURES

Fig. 1: Experimental setups used in this study: Batch experiments, 1-D diffusion experiments, and 2-D flow-through experiments.

Fig. 2: Photograph of the experimental setup used to perform the 1-D diffusion experiments (right panel) and schematics of system operation in different experimental phases, i.e., flow-through mode before starting the experiment (to achieve constant background concentrations) vs. no-flow conditions during the experiment (oxygen is allowed to diffuse into the system).

Fig. 3: Normalized iron(II)-concentration vs. time in the batch experiments performed (Table 1). Batch A: pH 7 (not buffered), Batch B: pH 7 (buffered), Batch C: pH 8 (buffered), Batch D: pH 7 (buffered) and with catalyzer.

Fig. 4: Observed and simulated evolution of (a) iron(II), (b) oxygen, and (c) pH in the Batch B experiment.

Fig. 5: Oxygen concentration profiles in the conservative 1-D diffusion experiment using glass beads as porous medium: (a) Spatial profiles measured at increasing times (i.e., in 3 to 6 hour-time intervals) along the oxygen-sensitive sensor strip. The depth = 0 mm indicates the location of the unsaturated/saturated interface. (b) Oxygen breakthrough curve at 13 mm depth below the interface between the atmosphere and the fully water-saturated porous medium (symbols indicate the experimental data and are shown at lower temporal resolution than the actual measurements, performed every 10 s).

Fig. 6: Spatial oxygen concentration profiles in the 1-D diffusion experiments: (a) Conservative case, (b) reactive case with kinetic iron(II) oxidation, and (c) instantaneous reaction. The depth of 0 mm indicates the location of the unsaturated/saturated interface.

Fig. 7: Diffusive oxygen fronts propagating in a pH-buffered porous medium over time: (a) Penetration depths for C_{norm} = 0.05 and (b) velocity of the propagating oxygen fronts.

749 Fig. 8: Temporal oxygen concentration profiles in the 1-D diffusion experiments (detected at 13 mm depth below the
750 interface between the atmosphere and the saturated porous medium) for the conservative, reactive kinetic, and
751 reactive instantaneous cases.
752
753 Fig. 9: Long-term propagation of oxygen concentration fronts in 1-D diffusive systems. Spatial profiles at (a) 0.5
754 days and 5.0 days, and at (b) 50 days and 500 days.
755
756 Fig. 10: 2-D flow-through experiment: (a) Photograph of the experimental setup during the reactive phase of the
757 experiment (with kinetic iron(II) oxidation and buffered pH), (b) simulated flow lines using MODPATH (Pollock,
758 1994) and color map showing the simulated precipitation of ferrihydrite (with maximum concentration close to the
759 inlet: 2.97×10^{-4} mol L^{-1} of bulk volume at 0.2 days). The vertical orange line shows the location of the vertical
760 oxygen-sensitive polymer strip (x = 13 cm). (c) Concentration profiles for the conservative and reactive experiments
761 (the y-axis represents the distance from the upper boundary of the flow-through setup).
762
763 Fig. 11: Penetration depth (a) and velocity of propagation of the dispersive oxygen fronts (b) in the quasi 2-D flow-
764 through setup as function of the longitudinal distance from the inlet of the flow-through chamber for two seepage
765 velocities (v = 1.9 and 0.19 m d^{-1}, respectively).

766 Table 1. Overview of the batch experiments.

Batch	Ferrous Iron, c(Fe^{2+})	Initial pH [-]	pH-buffer, c(PIPES)	Catalyzer, c(Cu^{2+})
A	1.79×10^{-4} mol L^{-1}	7	-	-
B	1.79×10^{-4} mol L^{-1}	7	1×10^{-3} mol L^{-1}	-
C	1.79×10^{-4} mol L^{-1}	8	1×10^{-3} mol L^{-1}	-
D	1.79×10^{-4} mol L^{-1}	7	1×10^{-3} mol L^{-1}	3×10^{-7} mol L^{-1}

767

768 Table 2. Summary of porous medium properties and flow and transport parameters in the 2-D setup.

Parameter	**Value**
Inner dimensions of the flow-through chamber, $L \times H \times W$ [cm]	16.2 × 12.7 × 0.5
Average grain diameter [mm]	0.50
Porosity of the porous medium [%]	39.7
Flow rate, Q [$m^3\ s^{-1}$]	5.63×10^{-9}
Cross-sectional flow-through area [m^2]	5.93×10^{-4}
Hydraulic conductivity, $\boldsymbol{K}$ [$m\ s^{-1}$]	2.5×10^{-3}
Aqueous diffusion coefficient for oxygen, D_{aq} [$m^2\ s^{-1}$] (at 22 °C)	1.97×10^{-9}

769

770 Table 3. Summary of parameters and results for the conservative experiments in the 1-D setup.

Porous medium	Glass beads	River Rhine sand
D_p **[m^2 s^{-1}]**	1.18×10^{-9}	1.14×10^{-9}
τ **(diffusion) [-]**	1.67	1.73
τ **(**ε**,** m **= 1.5) [-]**	1.57	1.52
ε **(porosity) [%]**	40.6	43.5

771

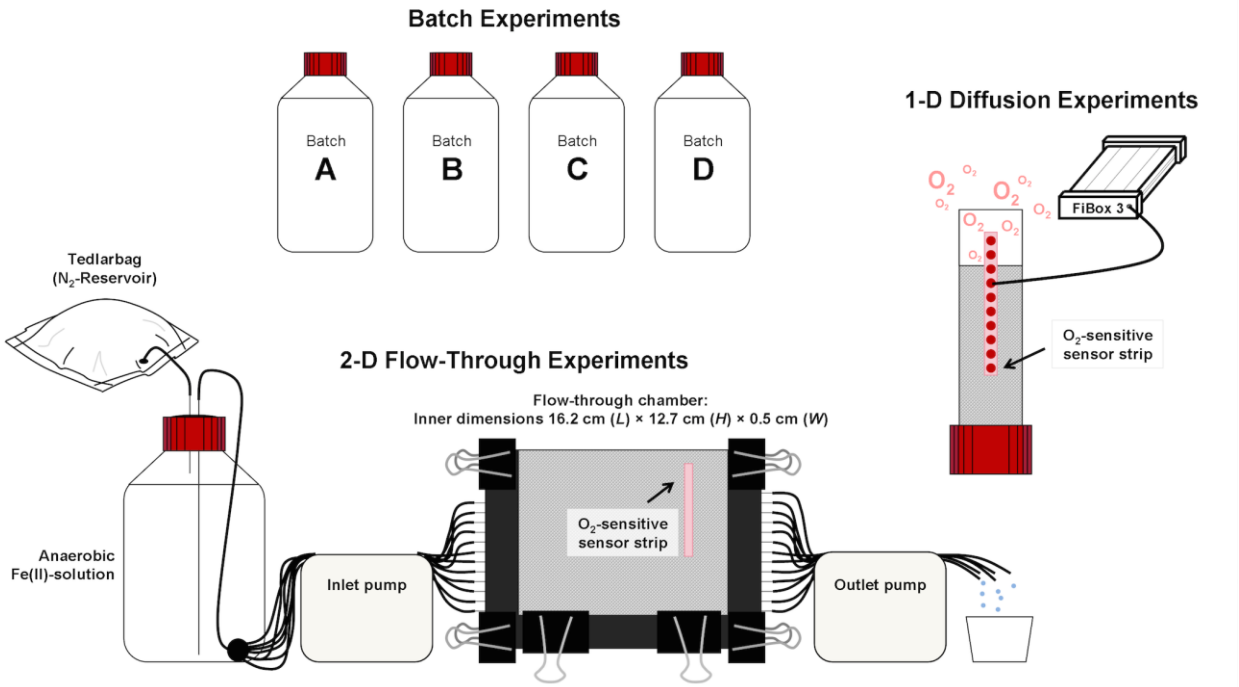

772 Fig. 1: Experimental setups used in this study: Batch experiments, 1-D diffusion experiments, and 2-D flow-through

773 experiments.

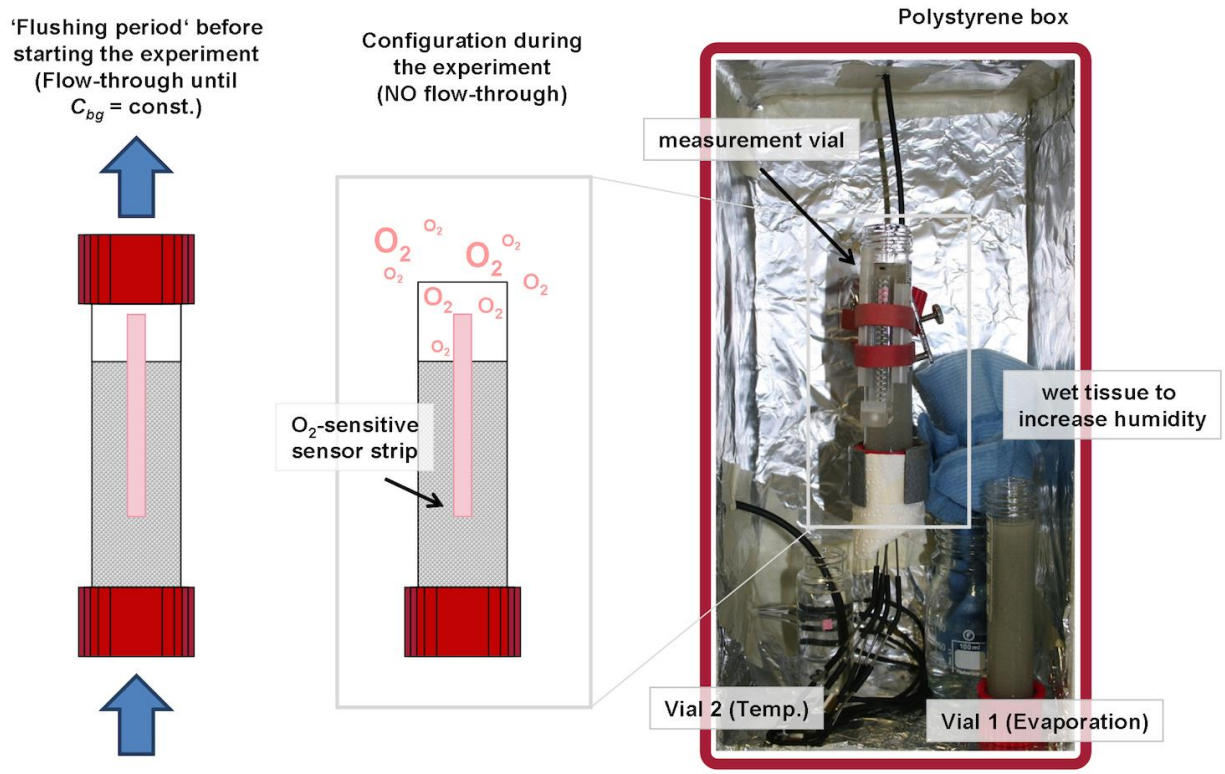

774

775 Fig. 2: Photograph of the experimental setup used to perform the 1-D diffusion experiments (right panel) and
776 schematics of system operation in different experimental phases, i.e., flow-through mode before starting the
777 experiment (to achieve constant background concentrations) vs. no-flow conditions during the experiment (oxygen is
778 allowed to diffuse into the system).

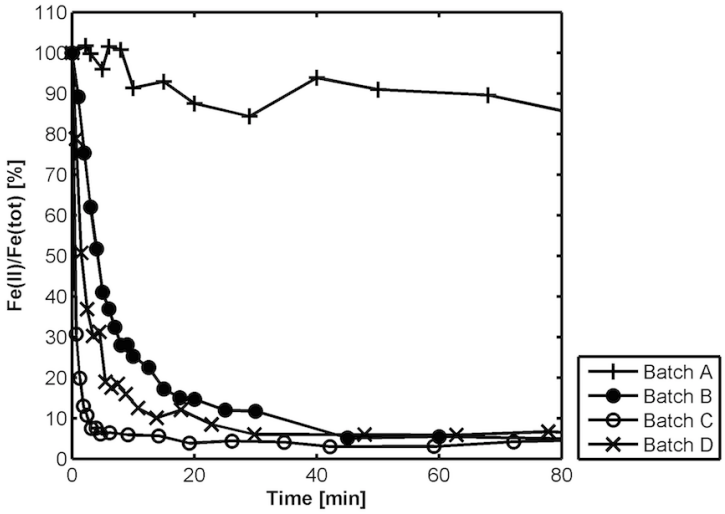

Fig. 3: Normalized iron(II)-concentration vs. time in the batch experiments performed (Table 1). Batch A: pH 7 (not buffered), Batch B: pH 7 (buffered), Batch C: pH 8 (buffered), Batch D: pH 7 (buffered) and with catalyzer.

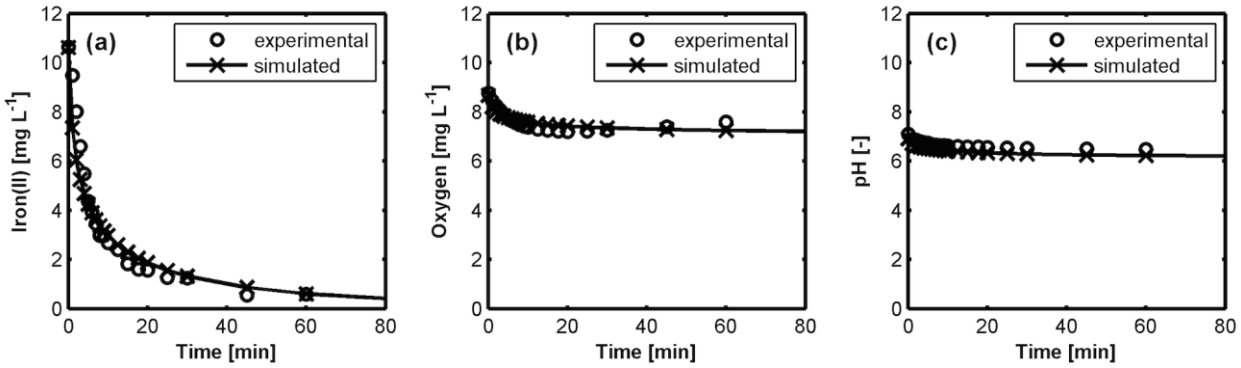

Fig. 4: Observed and simulated evolution of (a) iron(II), (b) oxygen, and (c) pH in the Batch B experiment.

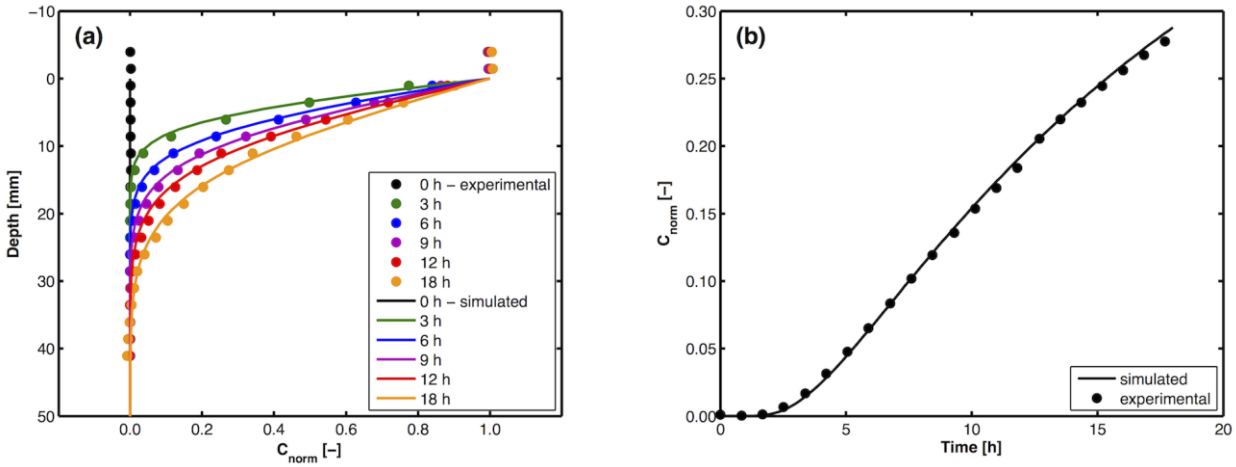

Fig. 5: Oxygen concentration profiles in the conservative 1-D diffusion experiment using glass beads as porous medium: (a) Spatial profiles measured at increasing times (i.e., in 3 to 6 hour-time intervals) along the oxygen-sensitive sensor strip. The depth = 0 mm indicates the location of the unsaturated/saturated interface. (b) Oxygen breakthrough curve at 13 mm depth below the interface between the atmosphere and the fully water-saturated porous medium (symbols indicate the experimental data and are shown at lower temporal resolution than the actual measurements, performed every 10 s).

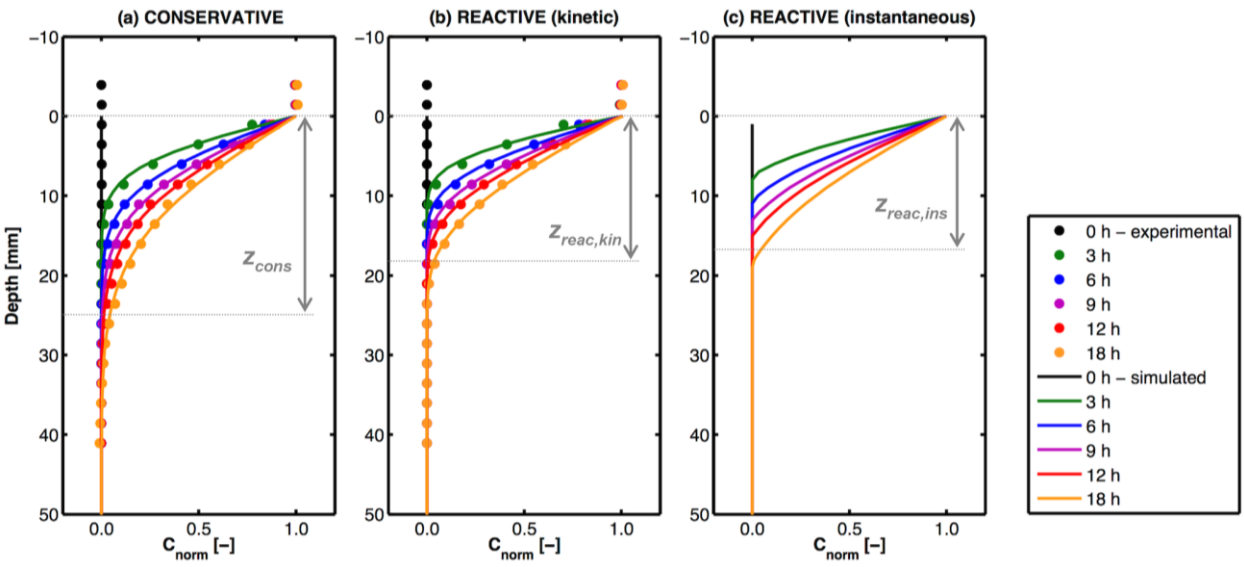

Fig. 6: Spatial oxygen concentration profiles in the 1-D diffusion experiments: (a) Conservative case, (b) reactive case with kinetic iron(II) oxidation, and (c) instantaneous reaction. The depth of 0 mm indicates the location of the unsaturated/saturated interface.

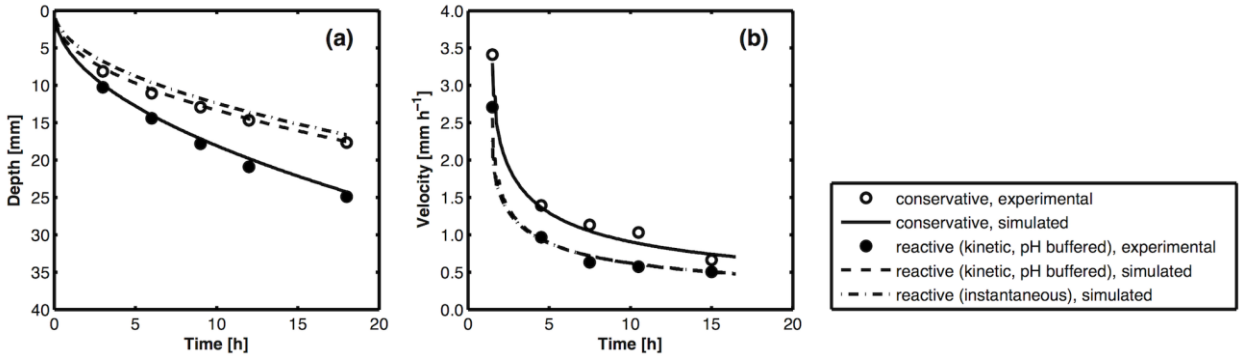

795

796 Fig. 7: Diffusive oxygen fronts propagating in a pH-buffered porous medium over time: (a) Penetration depths for

797 C_{norm} = 0.05 and (b) velocity of the propagating oxygen fronts.

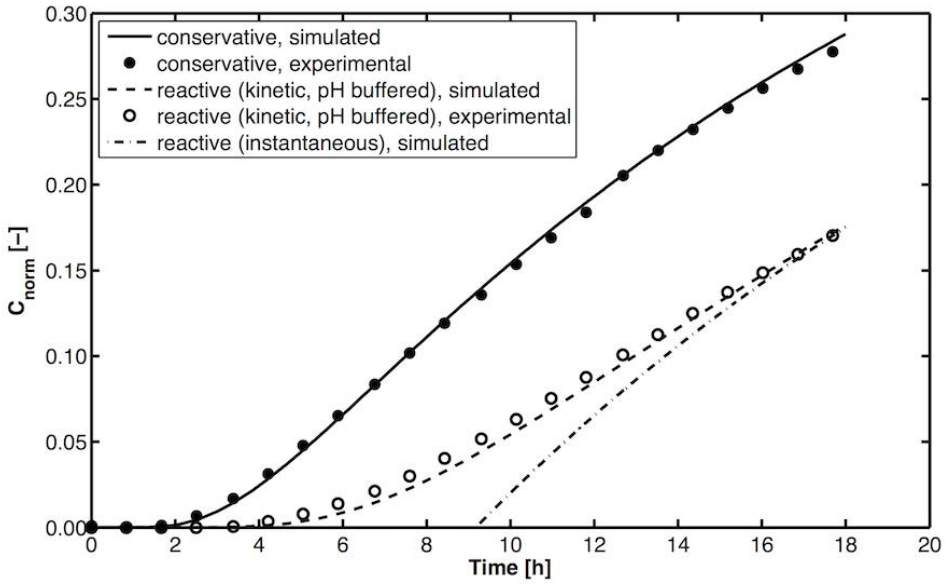

798

799 Fig. 8: Temporal oxygen concentration profiles in the 1-D diffusion experiments (detected at 13 mm depth below the
800 interface between the atmosphere and the saturated porous medium) for the conservative, reactive kinetic, and
801 reactive instantaneous cases.

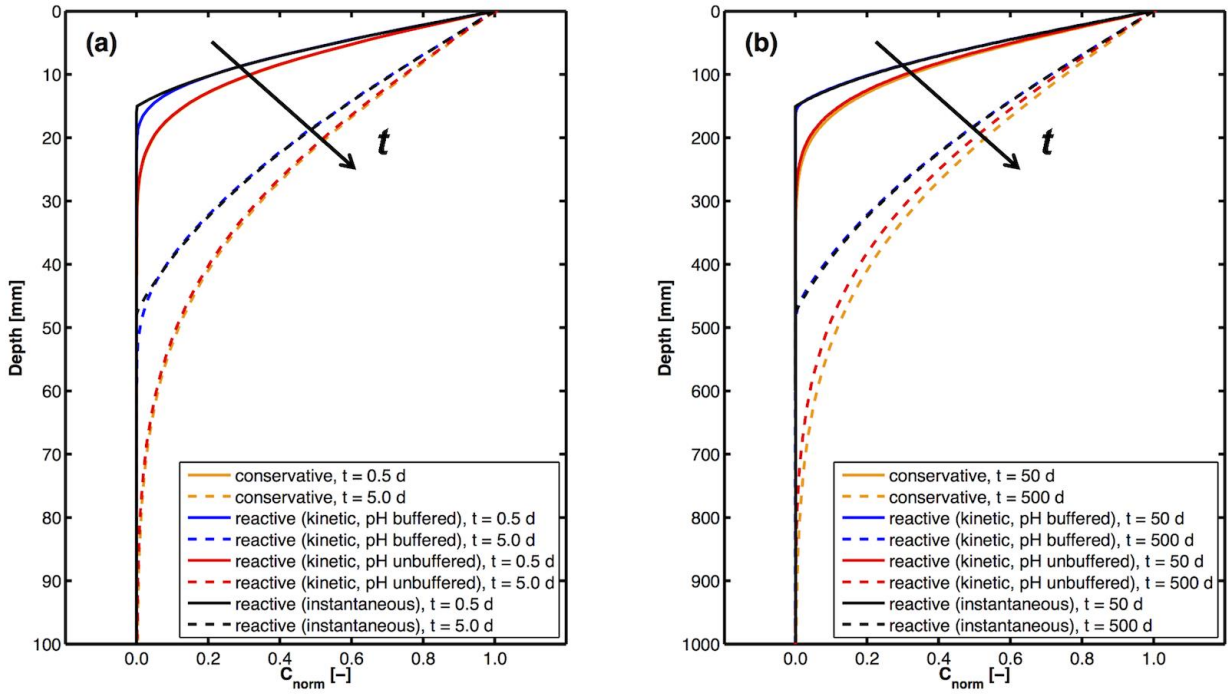

802

803 Fig. 9: Long-term propagation of oxygen concentration fronts in 1-D diffusive systems. Spatial profiles at (a) 0.5

804 days and 5.0 days, and at (b) 50 days and 500 days.

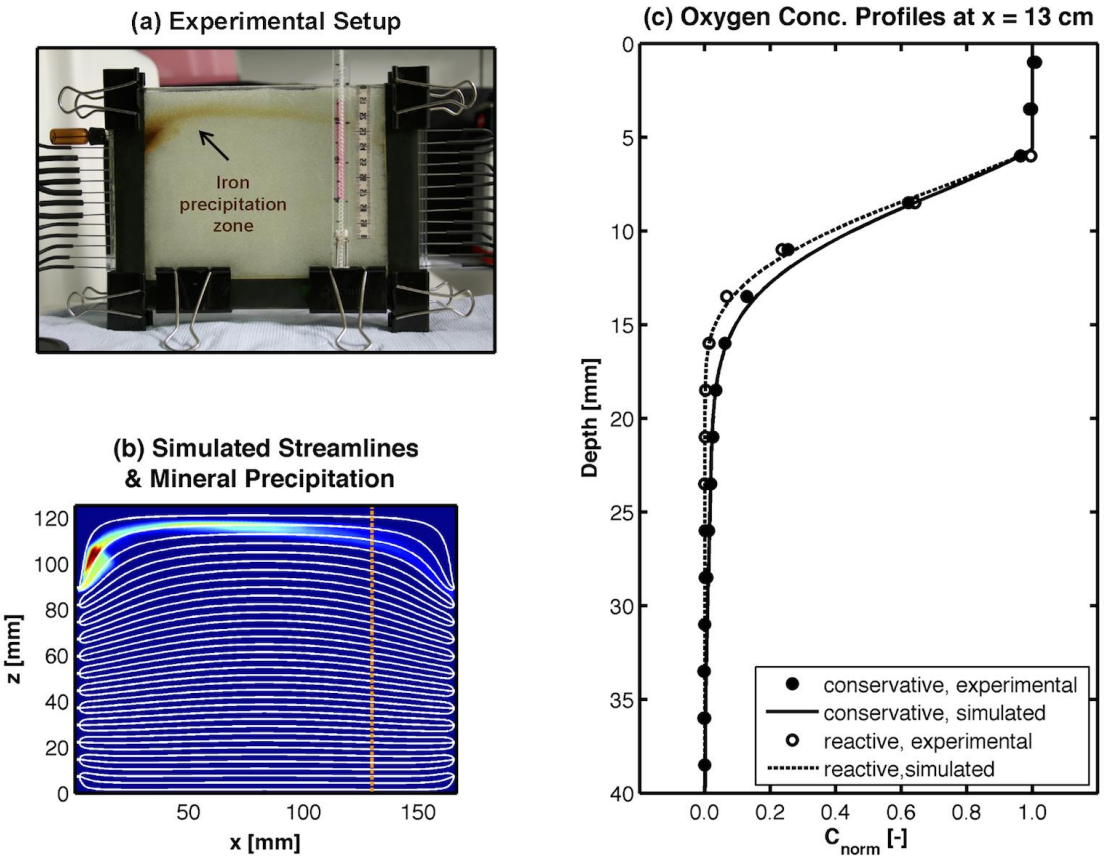

Fig. 10: 2-D flow-through experiment: (a) Photograph of the experimental setup during the reactive phase of the experiment (with kinetic iron(II) oxidation and buffered pH), (b) simulated flow lines using MODPATH (Pollock, 1994) and color map showing the simulated precipitation of ferrihydrite (with maximum concentration close to the inlet: 2.97×10^{-4} mol L^{-1} of bulk volume at 0.2 days). The vertical orange line shows the location of the vertical oxygen-sensitive polymer strip (x = 13 cm). (c) Concentration profiles for the conservative and reactive experiments (the y-axis represents the distance from the upper boundary of the flow-through setup).

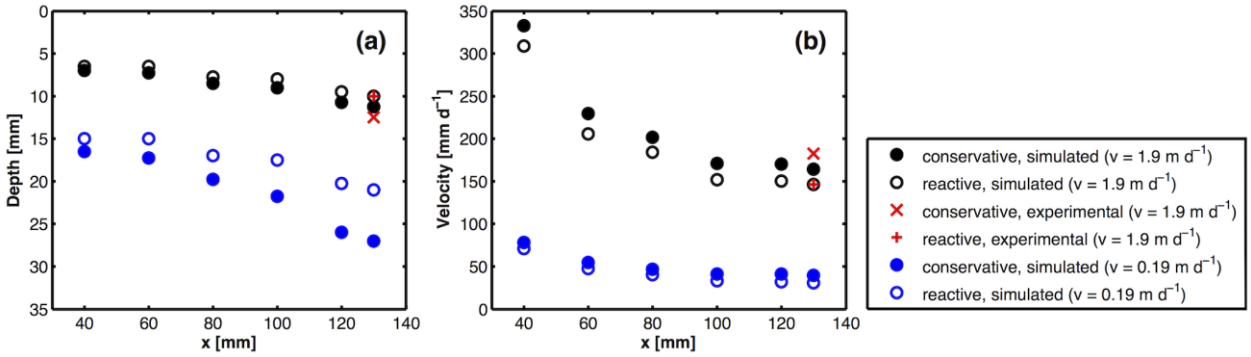

812

813 Fig. 11: Penetration depth (a) and velocity of propagation of the dispersive oxygen fronts (b) in the quasi 2-D flow-
814 through setup as function of the longitudinal distance from the inlet of the flow-through chamber for two seepage
815 velocities (v = 1.9 and 0.19 m d^{-1}, respectively).